A solver for simulating shock-induced combustion on curvilinear adaptive meshes

Han Peng, Chay W. C. Atkins, Ralf Deiterding*

School of Engineering, University of Southampton, Boldrewood Campus, SO16 7QF, United Kingdom

Abstract: A generic solver in a structured Cartesian adaptive mesh refinement framework is extended to simulate unsteady shock-induced combustion problems on a structured curvilinear mesh. A second-order accurate finite volume method is used with a grid-aligned Riemann solver for inviscid thermally perfect gas mixtures. To solve these reactive problems, detailed chemical kinetic mechanisms are employed with a splitting approach. The prolongation and restriction operators are modified to implement the adaptive mesh refinement algorithm on a mapped mesh. The developed solver is verified with several benchmark tests and is then used to simulate unsteady shock-induced combustion. The results show that the computed stand-off distance of waves and oscillation frequencies of mass fraction of products observed at the stagnation point are in good agreement with the results from experiments.

Keywords: adaptive refinement mesh, mapped meshes, reactive multispecies flow, shock-induced combustion

1. Introduction

Shock-induced combustion is a phenomenon where the combustion is self-ignited by a shock wave in a reactive mixture. The shock is typically driven by a wedge or a spherical projectile travelling at a high velocity, behind which the unburned mixture is compressed, and reactions are triggered. Shock-induced combustion is currently being extensively investigated as a promising combustion mode for supersonic and hypersonic airbreathing propulsion devices such as ram accelerator and oblique detonation wave engines [1, 2]. Hence, the complex coupling between shock wave and chemical reactions has been studied experimentally early to provide the understanding required to for the development of high-speed propulsion systems. One of classic studies is the ballistic experiment conducted by Lehr [3], in which a projectile was injected into a hydrogen/air mixture at

*Corresponding author: r.deiterding@soton.ac.uk

speeds around the Chapman-Jouguet (C-J) velocity. Under the unsteady condition, the combustion oscillates at regular periods between the bow shock and the projectile surface. In addition to the separation of leading bow shock wave and reaction wave, a corrugated reaction front was observed in the experimental schlieren images. McVey and Toong [4] proposed a wave interaction model to explain the mechanism of this unsteady shock-induced combustion. The model suggests that the combustion oscillates at a regular period consisting of several stages due to the wave interactions.

With the continued development of numerical methods and improvements in computational performance, numerical simulations have been increasingly used on unsteady shock-induced combustion problems [5-15]. The wave interaction model was numerically studied by Matsuo and Fujiwara [5] and by Wilson and Sussman [6] with a supplement mechanism about the effects of reflected shocks from the blunt body. In their studies, the reflected wave from the surface and the compression wave from a new reaction front overtakes the bow shock at approximately the same time. Numerical results based on detailed chemistry [7] indicate that the induction time is a key parameter for the frequency of the unsteadiness under subdetonative inflow. The concentration of heat release is a vital parameter for the unsteadiness itself. The compression waves created by increasing total energy depends on the amount of heat release itself. The process of unsteady shock-induced combustion is complicated due to multiple wave interactions; hence, this problem is considered as a good validation of reactive solvers [8-12].

As described, there are two main challenges for reliable simulations of unsteady shock-induced combustion. Firstly, the induction zone, namely the region between the bow shock and reaction front, should be accurately resolved. Its scale is reduced to the order of millimeters. A coarse mesh may cause unexpected coupling between bow shock and reaction wave, which could lead to unphysical oscillations. For this reason, more computational cells are needed in the induction zone to ensure the interactions among multiple waves can be correctly captured. Another challenge is the accurate prediction of the oscillation frequency, which is not only influenced by the wave interactions, but also determined by the induction time of chemical reactions. Therefore, most simulations of shock-induced combustion problems adopt detailed chemical-kinetic models to reproduce the experimental findings. Different chemical models were also studied numerically and it was shown that the selection of the reaction mechanism can be of crucial importance [13-15].

Adequate resolution of the induction region is essential to resolve the unsteady phenomena with detailed chemistry, but the calculation on a high mesh resolution is normally prohibitively expensive. The AMR (Adaptive Mesh Refinement) technique provides an approach to balance the computation accuracy and efficiency [16, 17]. The flow field can be refined at those places where there are large gradients of physical variables. Only a small number of studies on unsteady shock-induced combustion are published using the AMR technique [9, 10].

AMROC (Blockstructured Adaptive Mesh Refinement in object-oriented C++) [18] is an open-source framework based on a Cartesian mesh. The Clawpack package has been implemented into AMROC with an extended detailed chemical-kinetic model for multispecies thermally perfect gaseous mixtures. The generic solvers under this package have been widely used to study supersonic combustion and detonation problems [19-23]. The ghost fluid method and levelset method are presently used to deal with non-Cartesian boundaries. However, sometimes the levelset method is expensive, especially when the number of cut-off cells, i.e, the cells outside of the fluid domain, is large. Hence, it was decided to develop a solver on a quadrilateral but non-Cartesian mesh in AMROC. Using a body-fitted mesh can also avoid extremely small time steps, which may occur in some small cut cells. Recently, the solver on Cartesian grids in AMROC has been extended to work on body-fitted curvilinear grids for the LBM module [24] and the two-temperature finite volume module without AMR [25].

In this paper, a solver is implemented in AMROC-Clawpack to solve multispecies gaseous reactive problem on a mapped mesh with AMR. In Section 2, numerical methods and modifications to the Cartesian framework of AMROC-Clawpack are introduced. Section 3 first quantifies the numerical errors with the method of manufactured solutions and then presents the results of shock tube, shock box and detonation propagation problems by solving multi-component compressible Euler equations on a mapped mesh. In Section 4, the developed solver is validated by simulating the unsteady shock-induced combustion problems with different chemical-kinetic mechanisms. The frequencies of oscillation and stand-off distance of waves are presented. Finally, the conclusions and an outlook on future work are given in Section 5.

2. Numerical methods

2.1 Governing equations

The multi-species compressible Euler equations with a detailed chemical model in two-dimensional or axisymmetric form are solved as governing equations,

$$\frac{\partial \varpi_{\mathrm{a}} Q}{\partial t}+\frac{\partial \varpi_{\mathrm{a}} F_{\mathrm{C}}}{\partial x}+\frac{\partial \varpi_{\mathrm{a}} G_{\mathrm{C}}}{\partial y}=\varpi S_{\mathrm{axis}}+S\,, \tag{1}$$

$$Q=\begin{bmatrix}\rho_1\\ \vdots\\ \rho_{N\mathrm{sp}}\\ \rho u\\ \rho v\\ \rho E\end{bmatrix},\quad F_{\mathrm{C}}=\begin{bmatrix}\rho_1 u\\ \vdots\\ \rho_{N\mathrm{sp}} u\\ \rho u^2+p\\ \rho uv\\ (\rho E+p)u\end{bmatrix},\quad G_{\mathrm{C}}=\begin{bmatrix}\rho_1 v\\ \vdots\\ \rho_{N\mathrm{sp}} v\\ \rho uv\\ \rho v^2+p\\ (\rho E+p)v\end{bmatrix},\quad S_{\mathrm{axis}}=\begin{bmatrix}0\\ \vdots\\ 0\\ p\\ 0\\ 0\end{bmatrix},\quad S=\begin{bmatrix}\dot{\omega}_1\\ \vdots\\ \dot{\omega}_{N\mathrm{sp}}\\ 0\\ 0\\ 0\end{bmatrix}, \tag{2}$$

where Q are the conservative variables, F_{C} are the convective fluxes along the *x*-direction and G_{C} are the convective fluxes along the *y*-direction. S are chemical source terms, where i = 1, 2, …, N_{sp}. N_{sp} is the total species number, ρ_i is the density of component *i*. S_{axis} are axisymmetric source terms [26] activated by a parameter ϖ_{a},

$$\varpi_{\mathrm{a}}=(1-\varpi)+\varpi y\,, \tag{3}$$

where ϖ is a logical switch between two-dimensional (ϖ = 0) equations used in Section 3 and axisymmetric (ϖ = 1) equations used in Section 4. For simplicity, the following introduction is only based on the two-dimensional (ϖ = 0) equations in this section. The multi-species ideal gas state equation is used to close Equation (2),

$$p=\sum_{i=1}^{N_{\mathrm{sp}}}\rho_i\frac{\mathrm{R_u}}{W_i}T\,. \tag{4}$$

Besides, *E* in Equation (2) indicates the total specific energy,

$$E=\sum_{i=1}^{N_{\mathrm{sp}}}Y_i h_i-\frac{p}{\rho}+\frac{1}{2}\left(u^2+v^2\right), \tag{5}$$

where h_i is the specific enthalpy of species *i*,

$$h_i = h_{\text{ref}}^0 + \int_{T_{\text{ref}}}^{T} c_{\text{p}_i} dT \ . \tag{6}$$

The constant pressure specific heat c_{p_i} is dependent on temperature and calculated by the polynomial functions in the CHEMKIN II library [27]. $\dot{\omega}_i$ in Equation (2) is the mass generation rate of component *i*, which can be calculated by a chemical reaction mechanism of *J* steps as

$$\dot{\omega}_i = \sum_{j=1}^{J} \left(\nu_{ji}^r - \nu_{ji}^f\right) \left[k_j^f \prod_{n=1}^{N_{\text{sp}}} \left(\frac{\rho_n}{W_n}\right)^{\nu_{jn}^f} - k_j^r \prod_{n=1}^{N_{\text{sp}}} \left(\frac{\rho_n}{W_n}\right)^{\nu_{jn}^r} \right] \ , \ i = 1, \ldots N_{\text{sp}} \, . \tag{7}$$

The rate constant of forward and reverse chemical reaction is given by the Arrhenius formula:

$$k_j^{f/r}\left(T\right) = A_j^{f/r} T^{\beta_j^{f/r}} \exp\left(-\frac{E_j^{f/r}}{RT}\right). \tag{8}$$

The CHEMKIN II library [27] is incorporated into AMROC to solve the detailed chemical reactions and thermodynamic properties. A second-order accurate Strang splitting method is adopted for the source term treatment and a semi-implicit generalized Runge–Kutta method of fourth order (GRK4A) is utilized for the integration of the chemical kinetics [18].

2.2 Finite volume method on a mapped mesh

Generally, there are two different approaches for the coordinate transformation. The first one is working in the computational space and uses transformed governing equations for the physical variables. The numerical method based on Cartesian mesh can then be used without change. The second one is working in the physical space and derives the finite volume method on the nonuniform mesh. The latter is adopted in AMROC for the finite volume method with a capacity function [28] on mapped structured meshes.

The coordinates of a uniform Cartesian mesh (ξ, η) in computational space are firstly mapped into the coordinates of a non-uniform, curvilinear structured mesh (x, y) in physical space by a mapping function. A cell-centered finite volume method is used to discretise the multi-component Euler equations in physical space as

$$\begin{aligned} Q_{ij}^{n+1} = Q_{ij}^n - \frac{\Delta t}{|C_{ij}|}[&(\tilde{F}_{i+1/2,\,j}^n \cdot \tilde{L}_{i+1/2,\,j} - \tilde{F}_{i-1/2,\,j}^n \cdot \tilde{L}_{i-1/2,\,j}) \\ &+ (\tilde{G}_{i,\,j+1/2}^n \cdot \tilde{L}_{i,\,j+1/2} - \tilde{G}_{i,\,j-1/2}^n \cdot \tilde{L}_{i,\,j-1/2})] + \Delta t \cdot S. \end{aligned} \tag{9}$$

$\left|C_{ij}\right|$ in Equation (9) is the area of the physical cell indexed (i, j), the fluxes with tilde are the flux per unit length normal to physical interfaces between these meshes. The L with tilde is the physical length of the interfaces. The unit physical flux can be calculated by the unit computational flux. For example, the unit physical flux $\tilde{F}^{n}_{i+1/2,\,j}$ normal to the edge between cells (i, j) and $(i+1, j)$ has a relationship with the unit computational flux $F^{n}_{i+1/2,\,j}$,

$$\tilde{F}^{n}_{i+1/2,\,j} \cdot \tilde{L}_{i+1/2,\,j} = F^{n}_{i+1/2,\,j} \cdot L_{i+1/2,\,j}\,. \tag{10}$$

The $\tilde{L}_{i+1/2,\,j}$ is the physical edge length and $L_{i+1/2,\,j}$ is the edge length in the computation mesh. For the unit computational flux we write

$$F^{n}_{i+1/2,j} = F(Q^{n,\,l}_{i+1/2,\,j},\ Q^{n,r}_{i+1/2,j})\,, \tag{11}$$

for whose approximation a numerical flux scheme is needed. The final discretized form of the governing equations in the code is given as,

$$\begin{aligned} Q^{n+1}_{ij} = Q^{n}_{ij} &- \frac{\Delta t}{\left|k_{ij}\right|\Delta\xi}(\tilde{F}^{n}_{i+1/2,\,j} \cdot \frac{\tilde{L}_{i+1/2,\,j}}{\Delta\eta} - \tilde{F}^{n}_{i-1/2,j} \cdot \frac{\tilde{L}_{i-1/2,\,j}}{\Delta\eta}) \\ &- \frac{\Delta t}{\left|k_{ij}\right|\Delta\eta}(\tilde{G}^{n}_{i,j+1/2} \cdot \frac{\tilde{L}_{i,\,j+1/2}}{\Delta\xi} - \tilde{G}^{n}_{i,j-1/2} \cdot \frac{\tilde{L}_{i,\,j-1/2}}{\Delta\xi}) + \Delta t \cdot S \end{aligned}\,, \tag{12}$$

where the capacity function $\left|k_{ij}\right|$ is the area ratio of the physical cell to the computational cell indexed (i, j).

2.3 Grid-aligned Riemann solver

The Advective Upstream Splitting Method (AUSM) flux scheme developed by Liou [29] is implemented in the mapped solver for calculating the inviscid fluxes. In addition, a hybrid Roe/HLL scheme [18] is also used in this paper with multidimensional entropy correction and mass fraction positivity correction.

For the mapped meshes, a transformation is required before computing the fluxes. The velocities in the Cartesian coordinate system in physical space are rotated to the normal or tangential direction of the physical cell face [3]. Here a transformation matrix T_S [30] is used to rotate the velocities and calculate the flux normal to the face. The unit physical flux can be computed as

$$\tilde{F}^{n}_{i+1/2,\,j} = T_{\mathrm{S}}^{-1} F\left(T_{\mathrm{S}} Q^{n,\,l}_{i+1/2,\,j},\ T_{\mathrm{S}} Q^{n,\,r}_{i+1/2,\,j}\right), \tag{13}$$

$$T_{\mathrm{S}} = \begin{bmatrix} 1 & 0 & 0 & 0 & 0 & 0 \\ 0 & \ddots & 0 & 0 & 0 & 0 \\ 0 & 0 & 1 & 0 & 0 & 0 \\ 0 & 0 & 0 & n_x & n_y & 0 \\ 0 & 0 & 0 & -n_y & n_x & 0 \\ 0 & 0 & 0 & 0 & 0 & 1 \end{bmatrix}. \tag{14}$$

After the computing, the inverse matrix T_{S}^{-1} is used to rotate the flux back to the Cartesian coordinate system in physical space.

2.4 MUSCL-Hancock method

For the mapped solver in AMROC, the MUSCL-Hancock approach is used for the inviscid flux reconstruction. The MUSCL part reconstructs primitive variables or conservative variables in space and the Hancock part is used to update the reconstructed variables by half a time step, resulting in a scheme that is second-order accurate in space as well as in time. The method is developed for a Cartesian mesh and needs to be modified to work on the mapped mesh. In AMROC, the reconstruction is carried out using gradients calculated on computational meshes. Considering the MUSCL reconstruction for the Cartesian mesh,

$$Q^{l,n}_{i,\,j} = Q^{n}_{i,j} - \frac{1}{2}\varepsilon_i (1+\omega)\delta_{i-1,j}\frac{\Delta x_{\mathrm{c}}}{2} - \frac{1}{2}\varepsilon_i (1-\omega)\delta_{i,j}\frac{\Delta x_{\mathrm{c}}}{2}, \tag{15}$$

$$Q^{r,n}_{i,j} = Q^{n}_{i,j} + \frac{1}{2}\varepsilon_i (1-\omega)\delta_{i-1,j}\frac{\Delta x_{\mathrm{c}}}{2} + \frac{1}{2}\varepsilon_i (1+\omega)\delta_{i,j}\frac{\Delta x_{\mathrm{c}}}{2}. \tag{16}$$

ε_i denotes the limiter and the Minmod limiter is used for all the cases in present work. The value of ω is set to 0 as a linear reconstruction. δ is the discrete gradient and an example is given by

$$\delta_{i,j} = \frac{Q_{i+1,j} - Q_{i,j}}{\Delta x_{\mathrm{c}}}. \tag{17}$$

Δx_{c} is the interval between the centre of cell (i, j) and cell (i+1, j). In the computational space, namely on a Cartesian mesh, Δx_{c} is uniform and equal to the mesh size. However, for the mapped mesh, the physical interval should be taken into account in Equation (17) with a piecewise linear approximation. The modified gradient for the mapped mesh is therefore,

$$\delta_{i,j}=\frac{Q_{i+1,j}-Q_{i,j}}{L^{-}_{i+1,j}+L^{+}_{i,j}}. \tag{18}$$

$L^{+}_{i,j}$ is the interval between the centroid of cell (i, j) and the centroid of the interface (i+1/2, j) in physical space. $L^{-}_{i,j}$ is the distance between the centroid of cell (i, j) and the interface (i-1/2, j). Similarly, $L^{-}_{i+1,j}$ is the distance between the centroid of cell (i+1, j) and interface (i+1/2, j). The MUSCL reconstruction for the mapped mesh is given as,

$$Q^{l,n}_{i,j}=Q^{n}_{i,j}-\frac{1}{2}\varepsilon_i(1+\omega)\frac{(Q_{i,j}-Q_{i-1,j})L^{-}_{i,j}}{L^{+}_{i-1,j}+L^{-}_{i,j}}-\frac{1}{2}\varepsilon_i(1-\omega)\frac{(Q_{i+1,j}-Q_{i,j})L^{+}_{i,j}}{L^{-}_{i+1,j}+L^{+}_{i,j}}, \tag{19}$$

$$Q^{r,n}_{i,j}=Q^{n}_{i,j}+\frac{1}{2}\varepsilon_i(1-\omega)\frac{(Q_{i,j}-Q_{i-1,j})L^{-}_{i,j}}{L^{+}_{i-1,j}+L^{-}_{i,j}}+\frac{1}{2}\varepsilon_i(1+\omega)\frac{(Q_{i+1,j}-Q_{i,j})L^{+}_{i,j}}{L^{-}_{i+1,j}+L^{+}_{i,j}}. \tag{20}$$

A similar correction on the mapped mesh for the reconstruction can be found in Ref. [28].

2.5 Adaptive mesh refinement

AMROC currently adopts the block-structured adaptive mesh refinement technique (SAMR) proposed by Berger and Colella [16]. This technique uses a patch-wise refinement strategy. The meshes are firstly flagged by prescribed refinement criteria. Then, these flagged cells are clustered into an area of rectangular blocks of different sizes. The refined meshes are derived from their coarser parent meshes and finally an entire hierarchy of multi-level embedded grid patches is built [18].

One benefit of the Berger–Colella AMR method is that the main integrator is separated from the adaptive strategy. The numerical schemes are employed on grids at different levels. In the mapped solver, the data layout in AMROC remains unchanged and the entire AMR algorithm can be applied to the curvilinear structured mesh [32, 33]. For example, the coordinates of the flagged uniform Cartesian mesh in computational space (ξ_l, η_l) are refined or coarsened to generate the coordinates of grids at a higher level (ξ_{l+1}, η_{l+1}) or a lower level (ξ_{l-1}, η_{l-1}), respectively. By using the same mapping strategy, the new coordinates in computational space ($\xi_{l\pm1}$, $\eta_{l\pm1}$) are used to generate curvilinear structured grids in physical space ($x_{l\pm1}$, $y_{l\pm1}$) at the new level.

Several vital parameters are specified in the AMR algorithm. All the cases in the present work use

the following adaptive refinement parameters, unless otherwise stated. Refinement flags are always set and the grid hierarchy is recomposed in every coarser level time step, namely the value of regridding interval is set as 1. The bufferwidth is 2 to mark two additional cells around the flagged cells. The prescribed threshold for the clustering algorithm is set to 0.7, which means that the procedure generates successively smaller grids until the ratio between flagged and all cells in every new grid is above the given threshold.

2.5.1 Refinement criteria

In the present work, two different types of criteria are used to flag the grids. The first one is evaluating the differences between the adjacent cells. It can be considered as gradients multiplied by the step-size (named scaled gradients [10]) in all directions. Cell (i, j) is flagged if one of the inequalities

$$\begin{aligned}
&\left|w\left(Q_{i+1,j}\right)-w\left(Q_{i-1,j}\right)\right|>\varepsilon_w,\\
&\left|w\left(Q_{i,j+1}\right)-w\left(Q_{i,j-1}\right)\right|>\varepsilon_w,\\
&\left|w\left(Q_{i+1,j+1}\right)-w\left(Q_{i-1,j-1}\right)\right|>\varepsilon_w,\\
&\left|w\left(Q_{i+1,j-1}\right)-w\left(Q_{i-1,j+1}\right)\right|>\varepsilon_w
\end{aligned} \tag{21}$$

is satisfied for an arbitrary scalar quantity w, which is derived from the vector of state Q. The constant ε_w denotes a prescribed threshold value. This criterion is used for the adaptation along discontinuities in the flow field.

For regions of smooth solutions, the local truncation error is estimated by Richardson extrapolation [16] as another adaptation criterion. For simplicity, let $\mathrm{H}^{\Delta t}$ be a one-step explicit difference operator with time step Δt. The local truncation error of order o satisfies

$$Q(x,t+\Delta t)-\mathrm{H}^{\Delta t}\left(Q(x,t)\right)=\mathbb{C}\Delta t^{o+1}+O\left(\Delta t^{o+2}\right) \tag{22}$$

$\mathbb{C}$ is a constant in the leading-order term of the right-hand side (RHS). The second term of RHS $O\left(\Delta t^{o+2}\right)$ represents an error of the o+2 th order of magnitude. If Q is sufficiently smooth, the local error at t+Δt after two time steps with Δt is

$$Q(x,t+\Delta t)-\mathrm{H}_2^{\Delta t}\left(Q(x,t-\Delta t)\right)=2\mathbb{C}\Delta t^{o+1}+O\left(\Delta t^{o+2}\right), \tag{23}$$

and the local error at t+Δt after one time step with $2\Delta t$ is

$$Q(x,t+\Delta t)-\mathrm{H}^{2\Delta t}\left(Q(x,t-\Delta t)\right)=2^{o+1}\mathbb{C}\Delta t^{o+1}+O\left(\Delta t^{o+2}\right). \tag{24}$$

Subtracting (23) from (24) we obtain the relation

$$\mathrm{H}_2^{\Delta t}\left(Q(x,t-\Delta t)\right)-\mathrm{H}^{2\Delta t}\left(Q(x,t-\Delta t)\right)=\left(2^{o+1}-2\right)\mathbb{C}\Delta t^{o+1}+O\left(\Delta t^{o+2}\right). \tag{25}$$

Equation (25) is applied to estimate the leading-order term $\mathbb{C}\Delta t^{o+1}$ of the local error at $t+\Delta t$. The criterion based on this form requires a discrete solution $\mathbb{Q}(x,t-\Delta t)$ on a mesh two times coarser than the current mesh at level l. The restriction of $Q(x,t-\Delta t)$ is used to approximate the initial data on the coarser mesh. Then $Q(x,t)$ and $\mathbb{Q}(x,t-\Delta t)$ are updated as usual. Finally, a second coarsened solution $\bar{\mathbb{Q}}(x,t+\Delta t)$ is derived by prolongation of $Q(x,t+\Delta t)$. More details of the restriction and prolongation operators are given in Section 2.5.2. The leading-order term of the local error of quantity w is approximated by neglecting the high order terms in Equation (25),

$$\tau_{i,j}^{w}\approx\frac{\left|w\left(\bar{\mathbb{Q}}_{i,j}(x,t+\Delta t)\right)-w\left(\mathbb{Q}_{i,j}(x,t+\Delta t)\right)\right|}{2^{o+1}-2}. \tag{26}$$

The practical usage of τ^{w} is a combination with relative and absolute error,

$$\frac{\tau_{i,j}^{w}}{\max\left(w\left(\mathbb{Q}_{i,j}(x,t+\Delta t)\right),S_w\right)}>\eta_w. \tag{27}$$

S_w is the scaling factor for relative error of quantity w, which is an empirical parameter. In this paper, the relation (27) is used as a refinement criterion in terms of the mass fractions Y_i for the reactive problems. The scaling limit S_{Yi} is set as the 1% of the maximal value of the mass fractions Y_i in the C-J equilibrium state. If the relation (27) is satisfied, all four cells below the coarsened cell (i,j) are flagged for refinement.

Although the relative error criteria of multiple species are used for the reactive problems in this paper, it is recommended for users of AMROC to choose the mass fraction of the most relevant chemical species. The number of species criteria can be reduced if a strict temperature scalar gradient criterion is used. Based on the specific problems, there are different possible choices for the threshold. The user-specified threshold can be determined by running some test computations on a coarse mesh. More universal, sophisticated and efficient refinement criteria will be a potential improvement of the current strategy.

2.5.2 Restriction and prolongation

Transferring values from fine to coarse cells is called restriction in AMR algorithms. For Cartesian

restriction in AMROC, the value on a coarse cell is simply the average of its refined sub-cells, as displayed in Figure 1 (a). The average can be a conservative arithmetic mean because the area of the four fine cells are equal,

$$Q_{\mathrm{c}}=\frac{1}{n^2}\sum_{k=1}^{n^2}Q_{\mathrm{f},k}\ , \tag{28}$$

where subscript c denotes the coarse cell and the subscript f denotes the fine cell. The n is the refinement factor between these two levels. For the mapped mesh as shown in Figure 1 (b), the area weights of each fine cell should be counted to satisfy the conservation,

$$Q_{\mathrm{c}}=\frac{\sum_{k=1}^{n^2}A_{\mathrm{f},k}Q_{\mathrm{f},k}}{A_{\mathrm{c}}}\ , \tag{29}$$

where A is the area of each quadrilateral cell. An equivalent method is used in Ref [33], in which the weights of a capacity function are used in the restriction. It is noted that this restriction is conservative even though the overlapped refined cells are not exactly aligned with their coarse grid cells, but it may cause accuracy losses when the total area of refined cells are not equal to the area of their coarse grid cells.

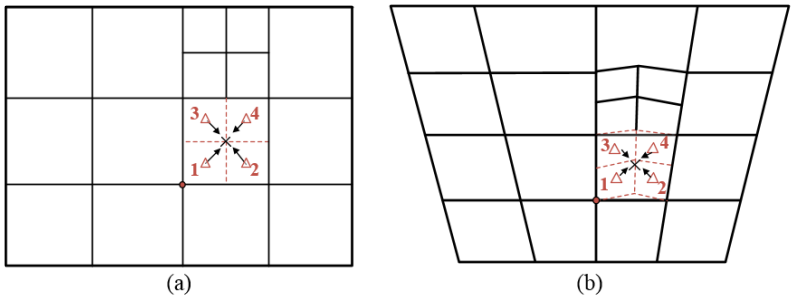

Figure 1. The restriction operator on (a) a Cartesian mesh, (b) a mapped mesh

Another important change for an AMR scheme on a mapped mesh is the prolongation operation from coarse to fine cells. For the Cartesian mesh, a bilinear space-interpolation is used in AMROC to pass the information from coarse to fine cells. The value of a newly refined cell is determined by the nearest four coarse cells, as shown in same colour in Figure 2 (a). For example, the value of the fine cell with the red solid triangle in its centre can be solved as

$$Q_{\mathrm{f}}=(1-f_1)(1-f_2)Q_{\mathrm{c},1}+f_1(1-f_2)Q_{\mathrm{c},2}+f_2(1-f_1)Q_{\mathrm{c},3}+f_1f_2Q_{\mathrm{c},4}\,. \tag{30}$$

The refinement factor in this figure is 2, so both the factors of f_1 and f_2 in the figure are 0.75. For the mapped mesh displayed in Figure 2 (b), the factors cannot be determined directly from the geometry. The physical coordinates of each cell centre are adopted to calculate the factors f_1 and f_2 by solving the nonlinear equations numerically,

$$\begin{cases} x_{\mathrm{f}}=(1-f_1)(1-f_2)x_{\mathrm{c},1}+f_1(1-f_2)x_{\mathrm{c},2}+f_2(1-f_1)x_{\mathrm{c},3}+f_1f_2x_{\mathrm{c},4} \\ y_{\mathrm{f}}=(1-f_1)(1-f_2)y_{\mathrm{c},1}+f_1(1-f_2)y_{\mathrm{c},2}+f_2(1-f_1)y_{\mathrm{c},3}+f_1f_2y_{\mathrm{c},4} \end{cases}. \tag{31}$$

The Newton-Raphson method [34] is used to solve the nonlinear equations. If this method is not convergent within given iteration steps, the gradient descent algorithm would be used. Then, Equation (30) is used to complete the prolongation.

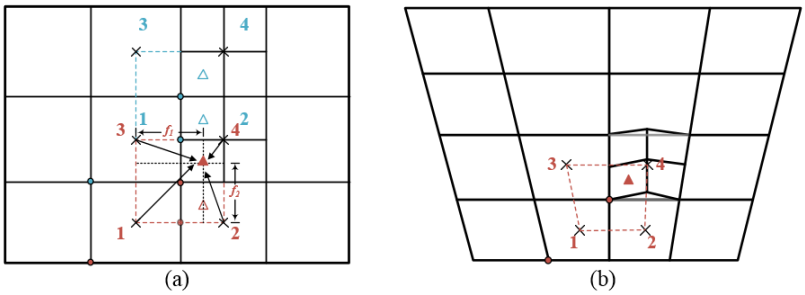

Figure 2. The prolongation operator on (a) a Cartesian mesh, (b) a mapped mesh

2.6 Boundary conditions

AMROC adopts the ghost cells approach to set the boundary conditions. The details of several types of boundary conditions used for Cartesian meshes can be found in Ref. [18]. Here the main differences are discussed when using a mapped mesh. The initialization in AMROC is conducted in the physical space, where the velocities are given in the Cartesian coordinate system in the physical space. As a result, the inflow and outflow boundary conditions are the same with those based on the Cartesian mesh. However, the symmetry and reflected wall boundary condition need to be transformed.

For a symmetry or inviscid wall boundary condition, the normal velocity at the physical boundary should be zero and there is no flow across the boundary. The transformation matrix T_{S} in Equation (14) is used to rotate the velocity of inner domain cells to align with the physical boundary. Then

the zero normal velocity condition is enforced by setting the value of the normal velocity in the ghost cell to be equal and opposite to the normal velocity in the domain cell. After that, the velocity in ghost cells is transformed back to the orthogonal direction of the Cartesian coordinate.

3. Numerical tests

In order to test the accuracy of the adaptive mapped method, three types of meshes are used in this section. The first one is a stretched mesh mapped by a clustering function [35],

$$\begin{cases} x = \xi \\ y = r_d * L_y \left[1 + \dfrac{\sinh\left[\beta(\eta - A)\right]}{\sinh(\beta A)} \right], A = \dfrac{1}{2\beta} \ln\left(\dfrac{1 + \left(e^{\beta} - 1\right) r_d}{1 + \left(e^{-\beta} - 1\right) r_d} \right) \end{cases}, \tag{32}$$

where the clustering factor β is 5 and the factor r_d is 0.5 for all the tests. L_y is the total length of the domain in the y-direction. The following function is used to generate a skewed mesh, where the angle of inclination is 15 degree in each direction:

$$\begin{cases} x = \xi + \eta \tan\left(\dfrac{\pi}{12}\right) \\ y = \eta + \xi \tan\left(\dfrac{\pi}{12}\right) \end{cases}. \tag{33}$$

In addition, a distorted mesh [36] is used in this case by applying

$$\begin{cases} x = \xi + L_x S_x \sin\left(\dfrac{2\pi\xi}{L_x}\right) \sin\left(\dfrac{2\pi\eta}{L_y}\right) \\ y = \eta + L_y S_y \sin\left(\dfrac{2\pi\xi}{L_x}\right) \sin\left(\dfrac{2\pi\eta}{L_y}\right) \end{cases}, \tag{34}$$

where the subscripts x and y denote the direction. L is the total length of the domain and S is the scaling factor in the respective direction. The scaling factor S is set as 0.075 for each direction. Both of these factors satisfy the constraint $0 \leq 2\pi S \leq 1$ to ensure that the mesh does not tangle. These three types of meshes are shown in Figure 3.

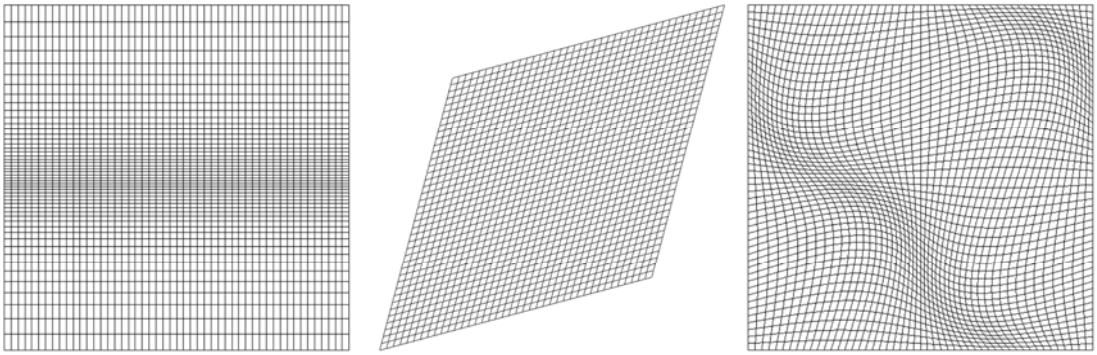

Figure 3. Schematic diagram of (a) a stretched mesh, (b) a skewed mesh and (c) a distorted mesh.

3.1 Method of manufactured solutions

In this subsection, the method of manufactured solutions (MMS) [37-38] is employed to verify the solver on different mapped meshes. The MMS has been used in many published studies to verify CFD codes and test the accuracy of the scheme. In the present solver, the chemical source terms are replaced by some analytical source terms to construct the Euler governing equations with manufactured solutions. The specific heat ratio is assumed to be a constant to simplify the derivation in terms of enthalpy in the analytical source terms. The general form of the solutions is given as:

$$\phi(x,y)=\phi_0+\phi_x f_{s,x}(a_{\phi_x}\pi x)+\phi_y f_{s,y}(a_{\phi_y}\pi y)\,. \tag{35}$$

ϕ denotes the variables and it could be density, velocity and temperature, etc. ϕ_0, ϕ_x, ϕ_y, a_x and a_y are constant. $f_{s,x}$ and $f_{s,y}$, are functions of sines and cosines. The detailed functions and coefficients are given in the appendix. The solutions are smoothly varying in the physical space.

One feature of the MMS is that the analytical solutions exist on arbitrary domains, so all the meshes introduced previously are tested in this case. The domain is set as [-150 cm, -30 cm] × [30 cm, 150 cm] in the computational space. Three refinement levels are utilized with refinement factor 2 for each level. The CFL number in this case is set to 0.1. The whole domain is initialized with a mixture of oxygen and nitrogen. A Dirichlet boundary condition is used for the inflow boundary and extrapolation is used for the supersonic outflow boundary.

Figure 4 gives an example where the mapped distorted mesh is a-priori refined at a specific region. The dynamic refinement is deactivated in this case to enable the comparison between analytical value and numerical solutions in the same cells. The fixed refinement also tests the operations for

information transfer between the fine mesh and coarse mesh.

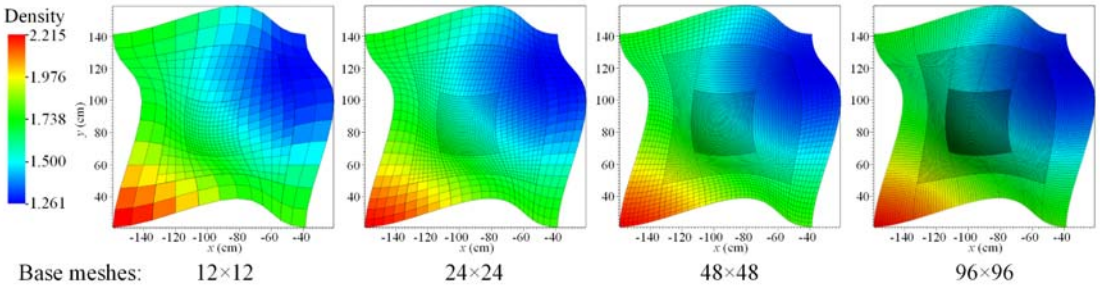

Figure 4. Statically refined distorted meshes and corresponding density distribution at t = 0.02 s.

The numerical solutions including density, mass fraction of oxygen, momentum and energy density are compared with analytical manufactured solutions. The errors in terms of the L_2 norm are shown in Figure 5. It can be observed that the numerical error decreases with the increasing number of base cells for each of the variables. This confirms that the present solver can achieve second order of accuracy when simulating the smoothly varying flow field on a hierarchically refined mapped mesh.

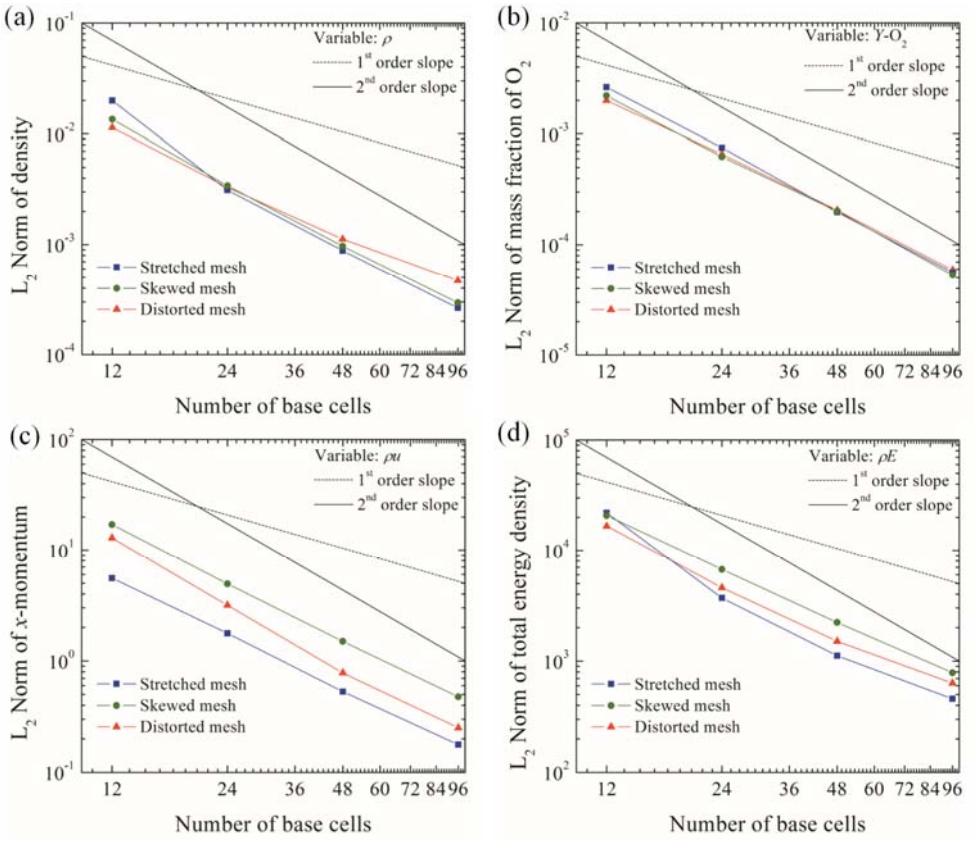

Figure 5. L_2 norm of (a) density, (b) mass fraction of oxygen, (c) *x*-momentum, (d) total energy density when using the MMS on different mapped meshes.

3.2 Multispecies shock tube

This benchmark is a modified version of Sod's shock tube considering a multi-species mixture. It has been used to verify the robustness of numerical schemes in previous work [39, 40]. In this case, a mixture of hydrogen–oxygen–argon at molar ratios 2:1:7 is initialized in the shock tube. A computational domain of 100 mm in length and of 50 mm in height is simulated with slip wall boundary conditions in all directions. For the adaptive cases, the base mesh contains 100 cells in the x-direction. The maximal refinement level is set as three with a uniform refinement factor of 2 on each level. The respective minimum mesh size is 0.25 mm in each direction. The refinement indicator threshold value ε_ρ is 0.005 kg/m^3 and ε_p is 1000 Pa. Correspondingly, in the cases without adaptive refinement, the same mesh resolution is used. The CFL number in this case is set to 0.5.

The initial conditions give a discontinuity of density and pressure in the middle of the tube (x =50 mm). The initial temperature and pressure are given by,

$$\begin{cases} T_\mathrm{L}=400\ \mathrm{K}, P_\mathrm{L}=8000\ \mathrm{Pa}, \text{ if } x \le 50\ \mathrm{mm} \\ T_\mathrm{R}=1200\ \mathrm{K}, P_\mathrm{R}=80000\ \mathrm{Pa}, \text{ otherwise} \end{cases}. \tag{36}$$

Figure 6 shows the density, horizontal velocity, temperature and the ratio of specific heats profiles along the centre line in the tube at 40 μs. The numerical results on different meshes are in good agreement with the results in Ref. [39, 40].

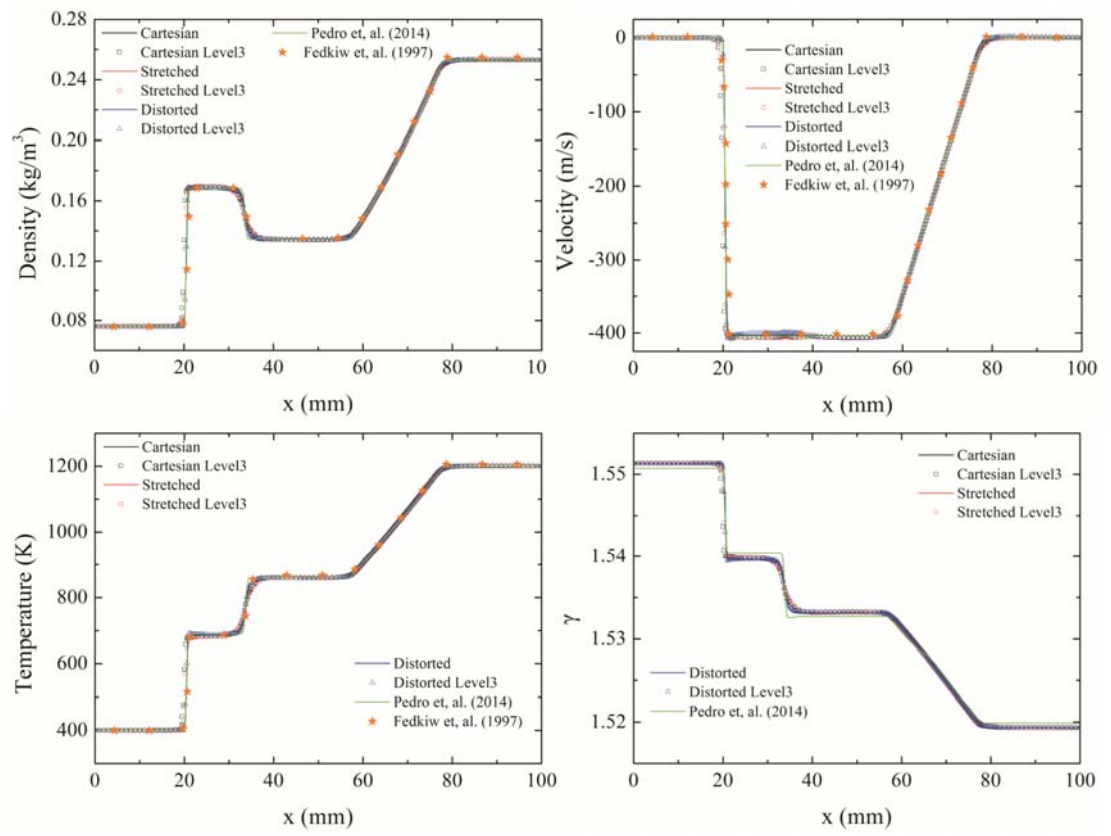

Figure 6. Numerical solutions of multispecies shock tube problem

3.3 Multispecies shock box

This benchmark is a modified two-dimensional Riemann problem in a shock box, which involves the interaction of multispecies shocks with slip walls [41]. The size of the shock box is 1000 mm × 1000 mm. The number of cells in the base mesh is 128 in each direction and three refinement levels are used with a uniform refinement factor of 2. The refinement indicator threshold ε_ρ is 0.05 kg/m^3 and ε_p is 16000 Pa. The CFL number in this case is set to 0.8. The whole domain is initialized with a mixture of oxygen and nitrogen at molar ratios 1:3.76. The initial condition is

$$\begin{cases} \rho_\mathrm{L} = 1.225\ \mathrm{kg/m^3}, P_\mathrm{L} = 101325\ \mathrm{Pa}, & \text{if } x \le 250\ \mathrm{mm} \text{ and } y \le 250\ \mathrm{mm} \\ \rho_\mathrm{R} = 4.9\ \mathrm{kg/m^3}, P_\mathrm{R} = 405300\ \mathrm{Pa}, & \text{otherwise} \end{cases}. \tag{37}$$

This condition gives two shock waves in each direction at the beginning, and then the shock waves propagate towards the slip walls. Figure 7 displays the results at 2 ms in computational space and physical space, respectively. This figure is overlapped by the base meshes with every 8th grid point for a better display and comparison. The convergent shocks are reflected by the lower-left corner.

The pressure and Mach number distributions are in good agreement with the results in Ref. [41]. The reflected shock wave is captured by the finest mesh as shown in Figure 8. The locally enlarged image shows how the distorted mesh is refined in this case.

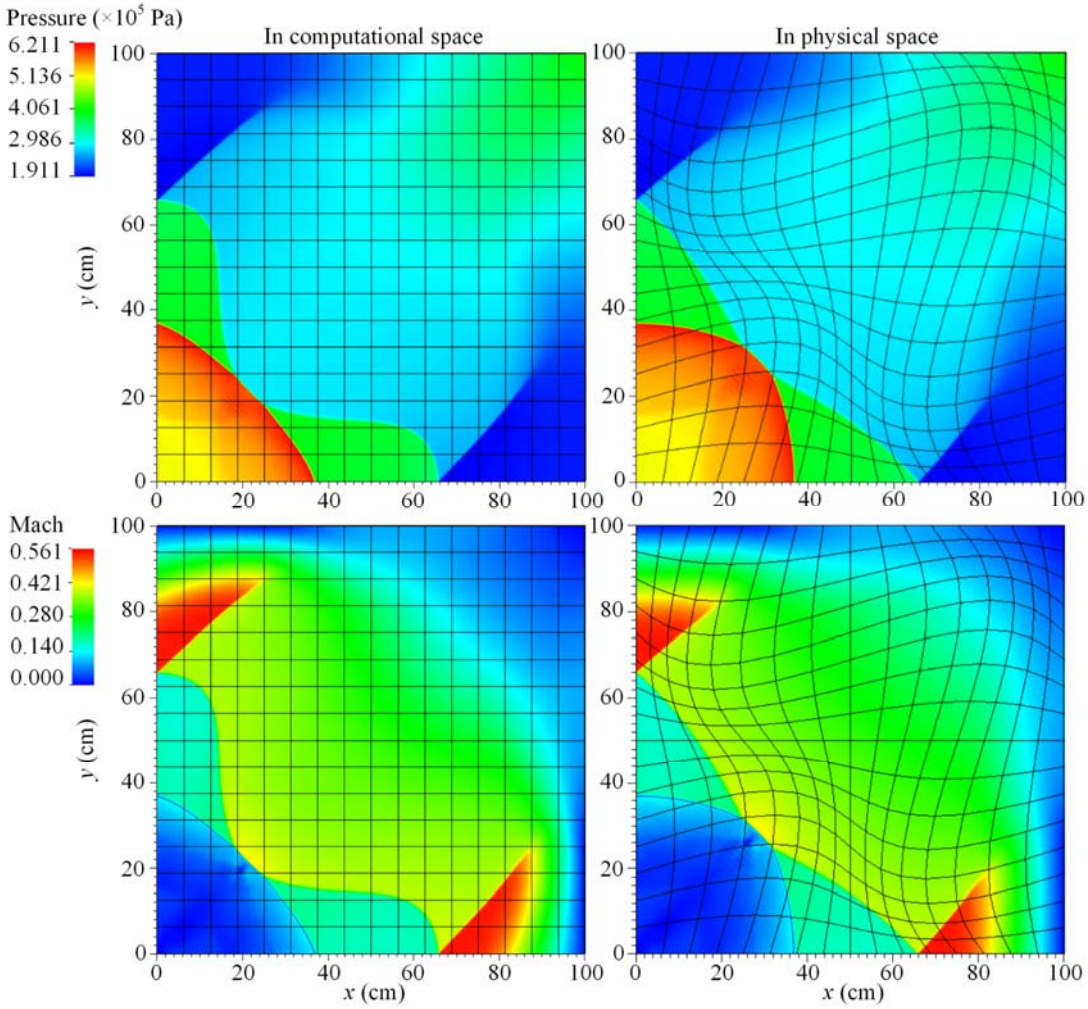

Figure 7. Numerical solutions of multispecies shock box problem

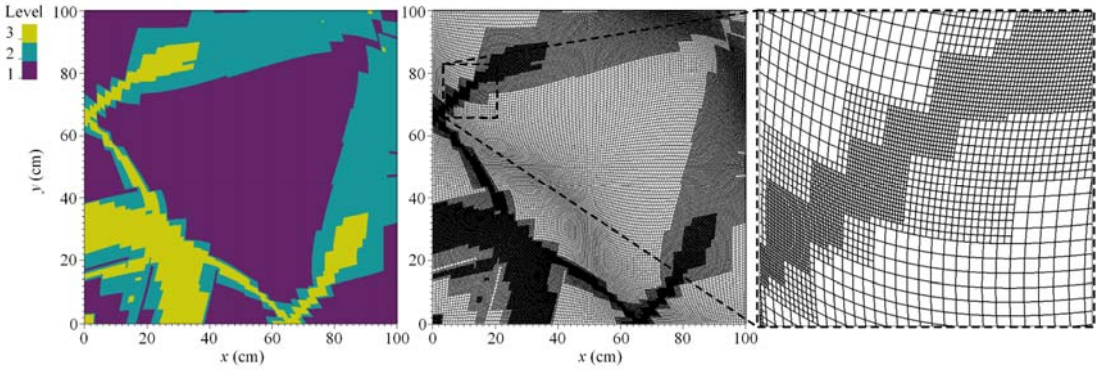

Figure 8. Pseudocolor image of the refinement levels and the image of the distorted refined mesh

3.4 2-D cellular detonation structure

Simulations of cellular detonation structure are conducted to test the accuracy of the reactive solver on a mapped mesh when chemically reactive source terms are present. The computational domain is a rectangular channel with a length of 1000 mm and a height of 32 mm. A mixture of hydrogen–oxygen–argon at molar ratios 2:1:7 is initialized in the channel. The initial temperature is 298 K and the pressure is 10 kPa. The one-dimensional detonation ZND solution for these parameters is used as planar initial conditions to establish a detonation wave in the left of the tube at location x=46 mm. An unreacted pocket is set behind the detonation front to generate an initial perturbation.

The detailed Westbrook hydrogen mechanism [42] is used in this case, which contains 9 species and 34 elementary reactions. The base mesh in this case is 2000×128 cells with five refinement levels. The refinement factor is 2 for each level. The induction length of the detonation is about 0.878 mm under the initial condition. Thus, the maximum resolution can be up to 56.2 Pts/lig (points per induction length) with the adaptive mesh. The refinement criteria are given in Table 1.

Table 1. Refinement indicators used for simulating cellular detonation structure

Refinement indicators	Species					
	H	H_2	O	O_2	OH	H_2O
S_Y ($\times 10^{-4}$)	0.2	1.2	1	10	1.3	8.5
η_Y ($\times 10^{-4}$)	5	2	5	2	5	1

The scaled gradient thresholds are given as, ε_T=500 K , ε_ρ=0.03 kg/m^3 , ε_p=40 kPa .

Figure 9 displays the detonation propagation on a Cartesian mesh and a stretched mesh. The detonation propagation velocity can be calculated through tracking the location of the maximum pressure gradient in the flow field. The numerical results show that the detonation velocity is around 1645.24 m/s on the Cartesian mesh and 1641.82 m/s on the stretched mesh, which is close to the C-J velocity 1629.34 m/s obtained by Cantera [43] and with the detonation toolbox [44]. The triple points are clearly resolved at the detonation front, where the transverse wave, Mach stem and the incident shock merge. A similar cellular structure is captured by the stretched mesh.

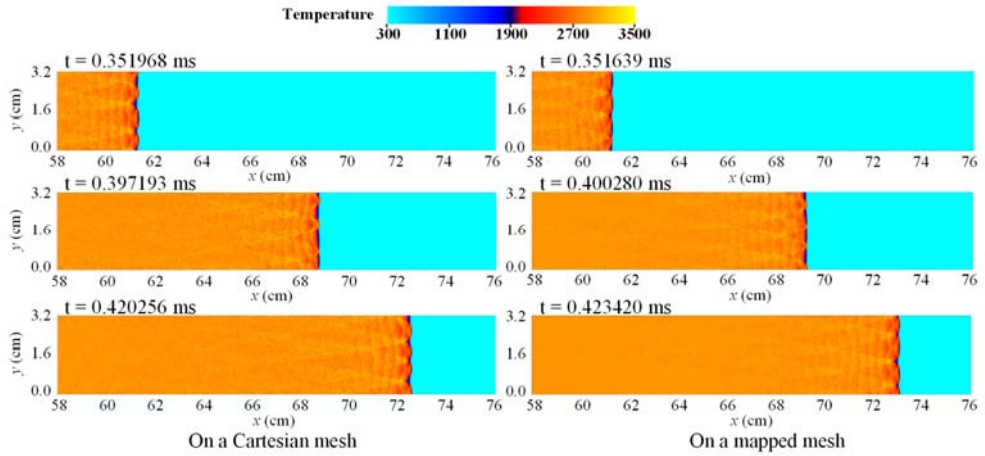

Figure 9. Numerical solutions of 2-D detonation propagation on a Cartesian mesh (left) and a stretched mapped mesh (right)

More detailed images of the stretched mesh are shown in Figure 10. The mesh is clustered at the centre of the tube. The whole detonation front and the slip lines behind are captured by the highest-level meshes. A locally enlarged image shows the triple point structure at the detonation front overlapped by non-uniform refined meshes. The opacity of the mesh is set as 50% to make a better display when the mesh is extremely dense.

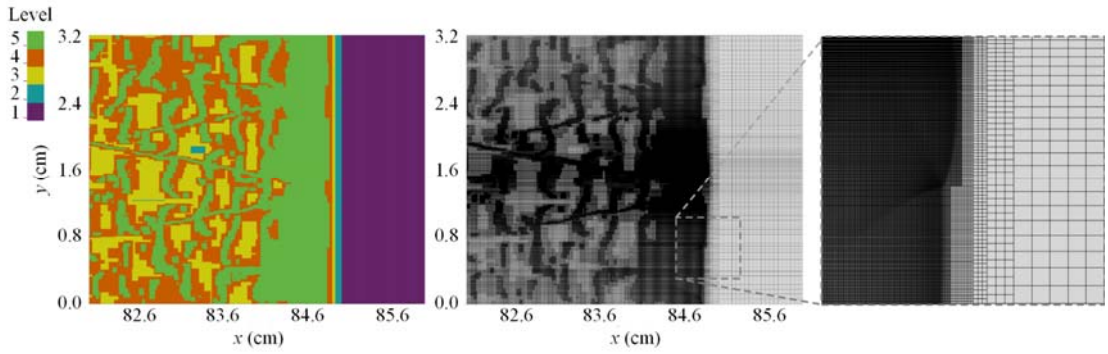

Figure 10. Pseudocolor image of the refinement levels and the image of the stretched refined mesh

The numerical detonation cells are illustrated by the trajectories of triple points in the flow field, which is captured by tracking the maximum of the vorticity in the whole domain on the base mesh. A detonation cell is a closed “fish-scale” pattern formed between two trajectories of triple points (seen in Figure 11). The numerical detonation cell size ranges from 8 to 10 mm, which is close to the value of 11.4 mm predicted by Cantera [43] with a correlation function [45]. However, the numerical cell size is much smaller than the experimental extrapolation value of around 40 mm [46] under the same initial condition. A similar lower prediction of detonation cell size in previous

published simulations [47, 48] are explained by the considerable heat loss at the channel walls in standard experiments [49].

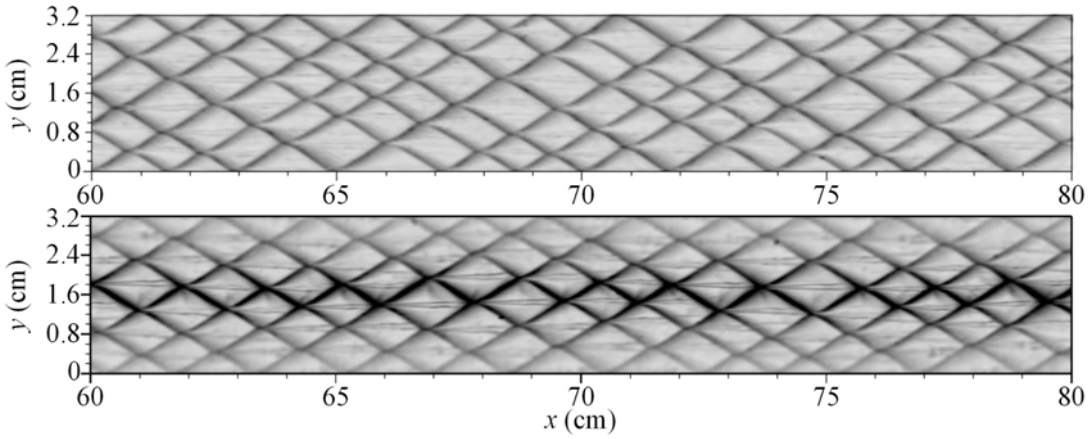

Figure 11. Trajectory of triple points on Cartesian mesh (top) and mapped mesh (bottom)

4. Unsteady shock-induced combustion

To simulate the unsteady shock-induced combustion phenomenon, the region in front of a blunt body is modelled according to Lehr's experiments [3] as displayed with blue color in Figure 12. For the axisymmetric problem, one half of this region is simulated by setting the bottom as a symmetry boundary. The base mesh is generated through the functions described in Ref [35],

$$\begin{cases} x = -\left(\left(r_{\mathrm{o}} - r_i\right) * \left(1-\xi\right) + r_{\mathrm{i}}\right) * \cos\left(0.5\eta\pi\right) \\ y = \left(\left(r_{\mathrm{o}} - r_i\right) * \left(1-\xi\right) + r_{\mathrm{i}}\right) * \sin\left(0.5\eta\pi\right) \\ r_{\mathrm{o}} = \sqrt{\left(r_{\mathrm{a}} * \cos\left(0.5\eta\pi\right)\right)^2 + \left(r_{\mathrm{b}} * \sin\left(0.5\eta\pi\right)\right)^2} \end{cases}, \tag{38}$$

where the inner radius r_i is 7.5 mm, the outer radius r_{a} is 11 mm in the *x*-direction and r_{b} is 15 mm in the *y*-direction. The computational domain is given as $\xi \in [0,1], \eta \in [0,1]$.

The supersonic flow consisting of a stoichiometric hydrogen-air mixture travels from left to right, which is equivalent to the blunt body moving with a supersonic speed. The right boundary is a supersonic outflow, where the values in external cells are extrapolated from the interior. The lower-right boundary is set as a slip wall. The initial temperature of the mixture is 293 K and the pressure is set as 42663.04 Pa. The modified Jachimowski's hydrogen/air mechanism is employed excluding nitrogen reactions [50]. This mechanism contains 9 species and 19 elementary reactions and has

been widely used in simulations for shock-induced hydrogen-air combustion [7, 12, 51-52].

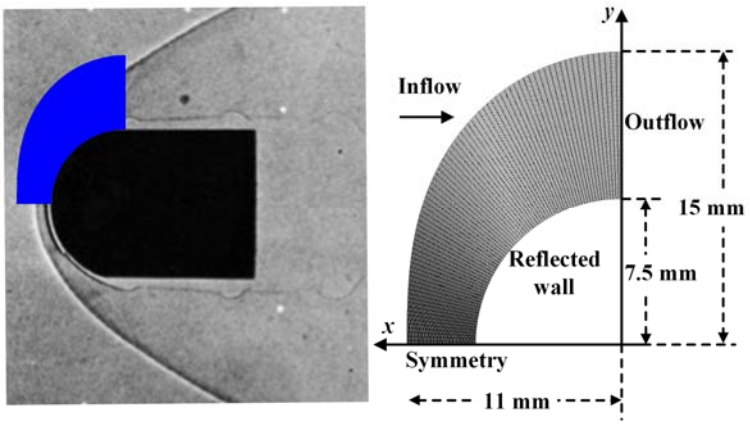

Figure 12. The physical model (left) [3] and computational domain (right)

To validate the mapped solver, Lehr's cases at Mach 4.18, Mach 4.48 and Mach 5.04 are simulated in this section. For the subdetonative cases, there are 250 base cells in the radial direction and 200 base cells in the circumferential direction, with 3 levels (refinement factors are 2, 2) adaptively refined on-the-fly. The refinement criteria are given in Table 2. The minimum radial mesh is about 3.5 μm and the minimum circumferential mesh is around 4.375 μm. For the Mach 5.04 case, the outer radius r_b of the domain is set to 16 mm in the *y*-direction to avoid the potential intersection of the bow shock and the inflow boundary. The number of base cells in the circumferential direction is up to 250.

Table 2. Refinement indicators used for simulating shock-induced combustion

Refinement	Species					
indicators	H	H_2	O	O_2	OH	H_2O
S_Y ($\times 10^{-4}$)	0.03	0.3	0.2	1.5	1.6	21.8
η_Y ($\times 10^{-4}$)	10	4	10	4	10	3

The scaled gradients are given as, ε_T=500 K , ε_ρ=0.02 kg/m^3 , ε_p=16 kPa .

4.1 Mesh dependency tests

For comparison, meshes with 2 levels and 4 levels of refinement are tested with the AUSM scheme to study the effect of mesh size on this problem. The case without refinement is also tested. The

regular oscillation of the bow shock wave and reaction front is one of the crucial parameters in unsteady shock-induced combustion. To illustrate the oscillation in the unsteady process, the temperatures and densities on the stagnation streamline are extracted at different times as shown in Figure 13. When the base mesh is used without AMR, the minimum mesh size is 14 μm. Under this mesh resolution, the reaction front oscillates at a lower frequency and the oscillation of the bow shock cannot be captured. When the mesh is refined, the locations of bow shock and reaction front oscillate regularly at a higher frequency, and the wave's stand-off distance is closer. In addition to the temperature distribution, the *x*-*t* diagram of the refinement level is also displayed in Figure 14. With the aid of Figure 13, it can be observed that all the oscillating bow shocks and reaction waves are dynamically captured by the highest-level mesh.

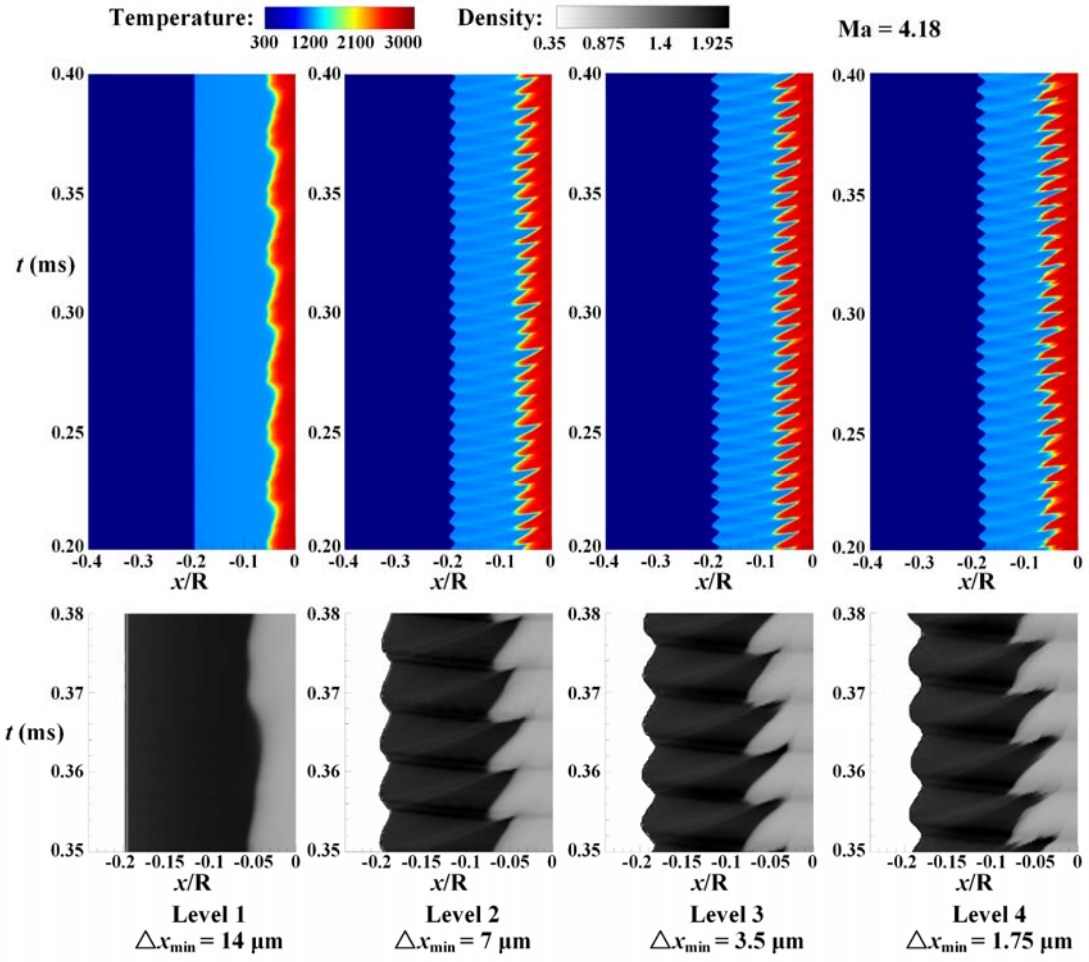

Figure 13. *x*-*t* diagrams of temperature on the stagnation streamline under different mesh resolution (top) and the enlarged *x*-*t* diagrams of density from 0.35 ms to 0.38 ms (bottom).

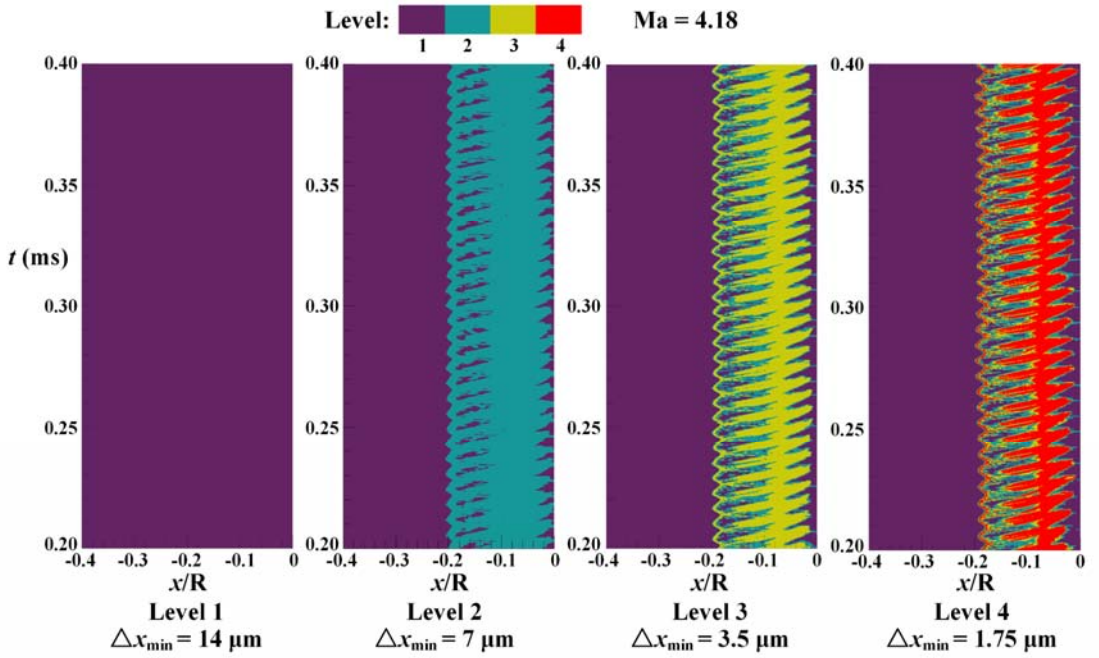

Figure 14. *x-t* diagrams of the domain of refinement levels (indicated by colour) on the stagnation streamline under different mesh resolution

In order to analyse the oscillation characteristics, the Fast Fourier Transform (FFT) is utilized. Due to the adaptive time step in the AMR solver, the time intervals for data processing are non-uniform. A linear interpolation is used to determine the mass fraction profiles from 0.2 ms to 0.4 ms with uniform time intervals. As a result, the frequency resolution is 5 kHz for all the cases. Figure 15 displays the frequencies of the water mass fraction oscillation at the stagnation point under different refinement levels. Similar to the results shown in Figure 13, only the coarsest mesh provides an incorrectly low frequency of 40 kHz. The frequency is convergent on a finer mesh. The frequency in the numerical solution is 160 kHz on a two-level or three-level refined mesh, which is close to the frequency, 148kHz, obtained in Lehr's experiment. Although a closer frequency 155 kHz can be obtained by increasing the mesh refinement level up to 4, the three-level refinement is considered as a good trade-off between the computational efficiency and cost. Therefore, all the meshes are refined with three levels in the following calculations.

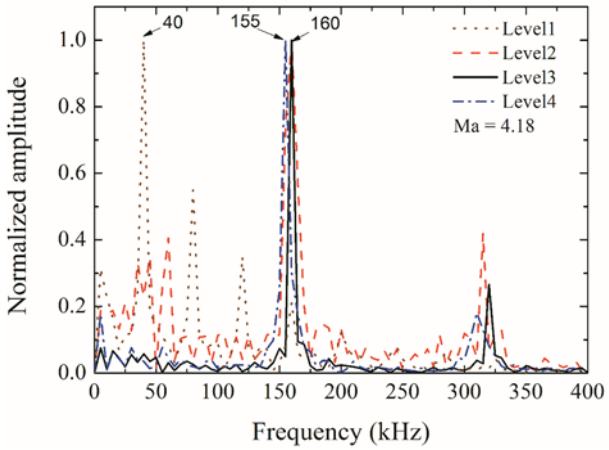

Figure 15. Frequencies of mass fraction of H_2O oscillation at the stagnation point under different mesh resolution

Table 3 gives timing data from present dynamically adaptive simulations versus uniform computations under the same mesh size. The benefit in computational costs from dynamic mesh adaptation is apparent when the mesh resolution is high. It should be pointed out that for such a classical problem, the chosen computational domain is already reduced to include all the potential physical features. The advantage of adaptive simulations is not remarkable when the number of cells is small.

Table 3. Comparison of uniformly refined and dynamically adaptive simulations for the shock-induced combustion problem at Mach 4.18 run on Intel Xeon E5-2670 processors from t =0 ms to t = 0.2ms

Ma = 4.18	Uniform		Adaptive	
Δx_{min} (μm)	Cells	Run time (cpu·h)	Level	Run time (cpu·h)
14	50,000	36.7		
7	200,000	240.0	2	308.6
3.5	800,000	1286.7	3	1193.5
1.75	3,200,000	9590.6	4	5521.6

Figure 16 shows a comparison between the numerical results calculated by the solver based on the AMR mapped mesh and Lehr's experiments. The numerical solutions are in good agreement with the experimental results. The shock-induced combustion is observed in front of the blunt body and

the bow shock stand-off distance is nearly the same as that in the experiments. The flame surface is also corrugated, due to the interaction of the waves in the flow field. It is noted that the experimental schlieren image at Mach 4.48 is taken at a 12° angle from the perpendicular direction, which provides a possible explanation why the reaction front location is slightly different to the experimental result.

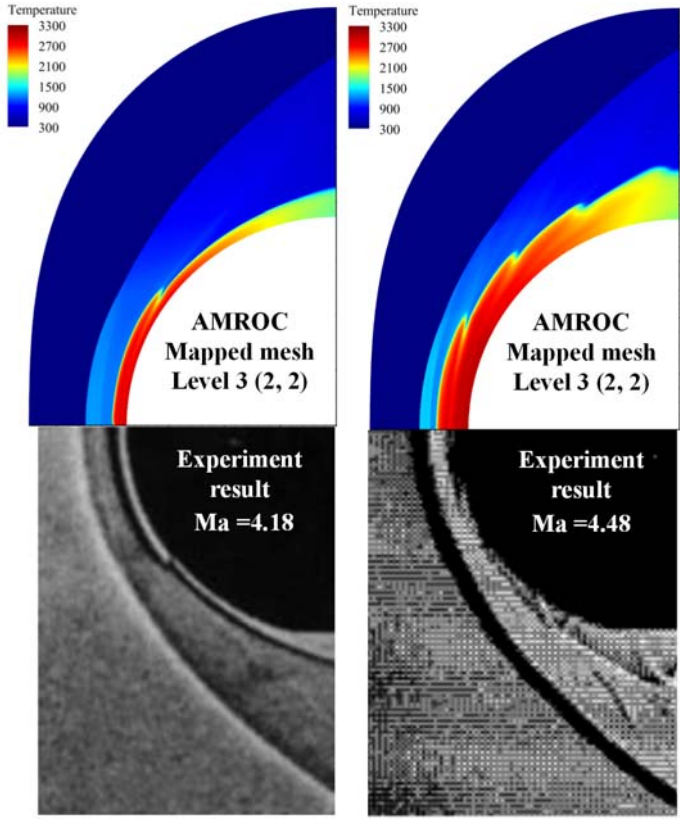

Figure 16. A comparison between the numerical temperature distribution from the AMR mapped mesh solver and the experimental schlieren images [3]

4.2 Refinement criteria tests

A more detailed two-dimensional structure can be seen in Figure 17 with the Roe/HLL scheme. The combustion is induced by the bow shock wave in front of the blunt body. Several typical characteristics can be inferred from the results. Firstly, the reaction wave is separated from the bow shock wave, while the reaction front is corrugated and unstable. Another feature is the existence of waves, i.e., the compression wave, reflected wave and contact discontinuity, between the bow shock wave and the reaction front. The interaction of waves and the stagnation surface of the blunt body has been considered as the source of the pressure and combustion oscillations.

The adaptively refined mapped mesh is also shown in Figure 17. All wave structures mentioned above are captured and refined by the finest mesh (Level 3 mesh). The enlarged region shows how the body-fitted mesh is refined near the bow shock and the reaction front. The region without shock wave and reactions uses the coarsest mesh, which effectively reduces the computational cost in the high-resolution simulations.

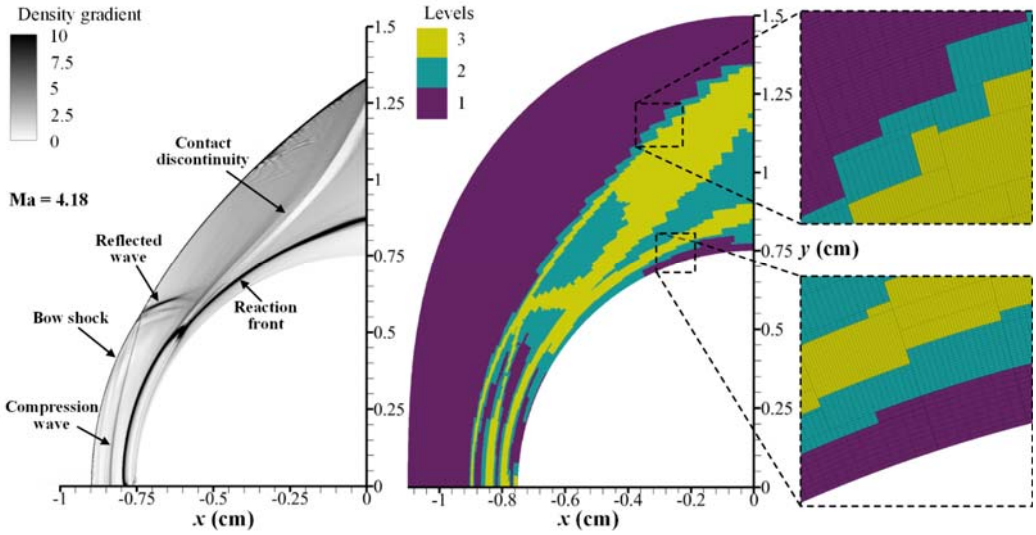

Figure 17. The density gradients and corresponding refinement levels distribution

In this section, a combination of the physical refinement indicators (seen in Table 2) is employed to flag the meshes for refinement as described in Section 2.5.1. In order to study the effects of refinement criteria on the simulations, the Mach 4.18 case is simulated on a three-level grid with Roe/HLL scheme. In addition to the refinement criterion used in Table 2 (Criterion-2), a looser (Criterion-1) and a stricter criterion (Criterion-3) are tested with different refinement indicators given in Table 4.

Table 4. Refinement indicator values used for simulating shock-induced steady combustion

Criterion	Computational cost (cpu·h)	Scalar gradient ε			Local truncation error η_Y ($\times 10^{-4}$)					
		T (K)	ρ (kg/m^3)	p (kPa)	H	H_2	O	O_2	OH	H_2O
1	974.2	1000	0.04	32	20	8	20	8	20	6
2	1622.8	500	0.02	16	10	4	10	4	10	3
3	2424.0	250	0.01	8	5	2	5	2	5	1.5

The scaling factors S_Y for all the three criteria are identically given as the same as in Table 2.

The iso-contours of these indicators on level 2 and corresponding density gradient distribution are depicted in Figure 18. The Criterion-1 case uses a relatively loose criterion, where the bow shock wave and reaction front are captured by the finest mesh. The indicators of scaled gradient of density and pressure are used to achieve adaptation to the shocks. The indicators of scaled gradient of temperature and the errors of mass fractions are employed to flag the reaction front and the compression waves near the stagnation line. In a stricter case (Criterion-2), the contact discontinuities are flagged to refine to the finest meshes. The Criterion-3 case uses the strictest refinement indicators, and a large part of the region behind the bow shock is unnecessarily refined to the highest level.

The scaled gradient of density has a vital influence on flagging the region without shock and flame but with contact discontinuities. A suitable criterion should ensure that all the main physical features are captured by the finest mesh, meanwhile the flagged meshes should be as few as possible. Table 4 also shows that the computational cost increases obviously when more meshes are refined. Considering the balance of accuracy and computational cost, the set of refinement indicators in Table 2 (Criterion-2) is appropriate, and all the following cases adopt this criterion.

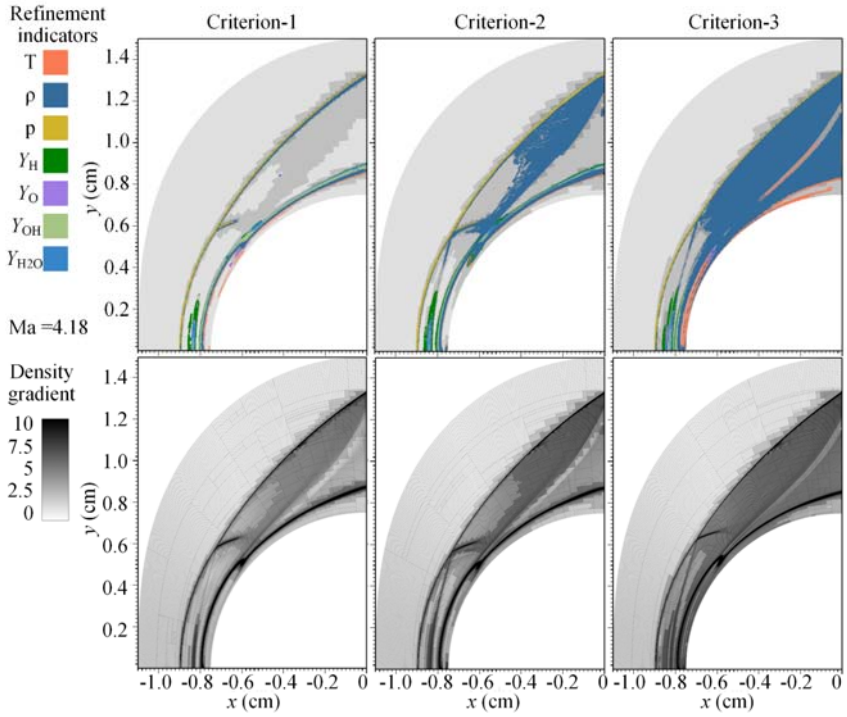

Figure 18. Active refinement indicators on level 2 and the density gradients distribution under different refinement criteria for a 3-level computation

4.3 Chemical mechanism tests

In addition to using the Jachimowski mechanism, the UCSD hydrogen/air mechanism [53] is also used in the tests on a mapped mesh with 3 levels of refinement. As seen in Figure 19, both reaction models predict a regular oscillation at Mach 4.18. Compared with the Roe/HLL scheme, the AUSM scheme provides more regular oscillations. The difference is small between these two schemes in predicting the locations of shock wave and reaction front with the same chemical mechanism.

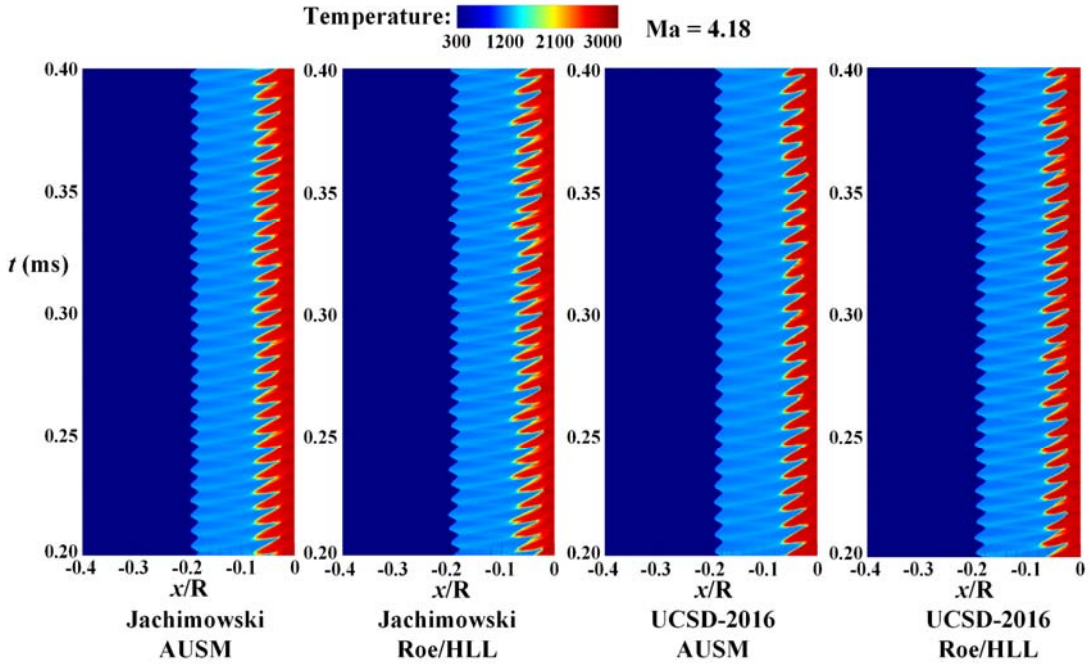

Figure 19. *x*-*t* diagram of temperature along the stagnation streamline at Mach 4.18 on a three-level refined mapped mesh

Figure 20 shows that an instability mode is observed both in the AUSM and Roe/HLL cases with the UCSD model when the inflow Mach is 4.48. The high frequency oscillation is coupled with a relatively low frequency on this mode, whereas the Jachimowski model still gives a stable high frequency oscillation. Some previous work [14, 15] has reported this unstable phenomenon with different chemical mechanisms.

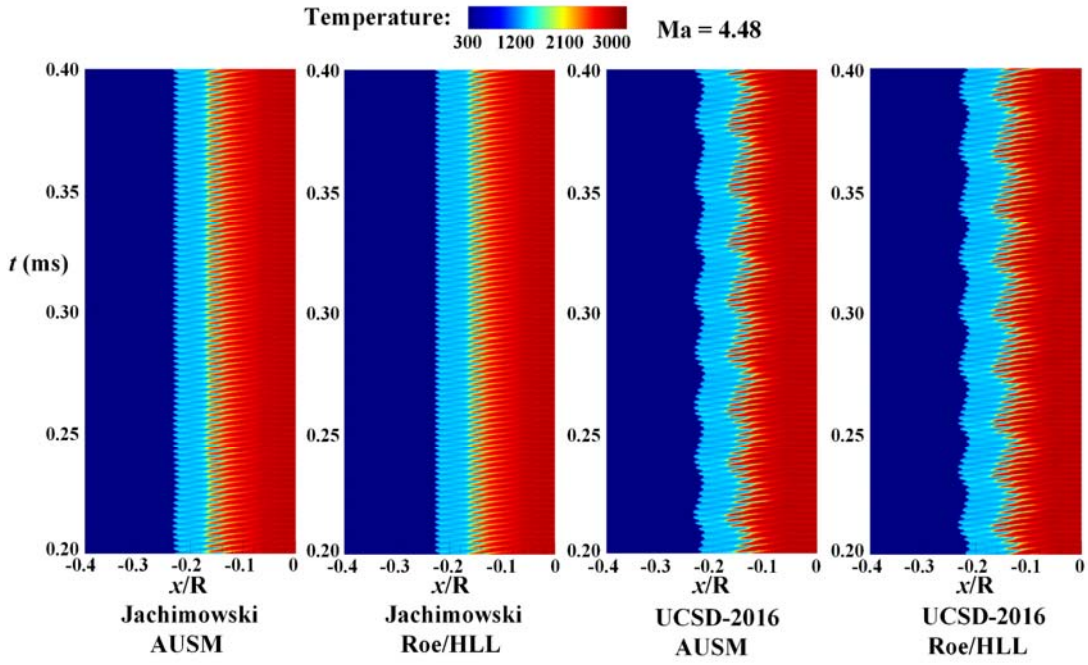

Figure 20. *x-t* diagram of temperature along the stagnation streamline at Mach 4.48 on a three-level refined mapped mesh

As shown in Table 5, the Jachimowski model predicts that the frequency of oscillation is 160-165 kHz, determined by the FFT method as mentioned previously. The UCSD model gives a frequency of 145-155 kHz, which is closer to the experimental frequency of 148 kHz. For the Mach 4.48 case, a relatively low frequency is observed when using the UCSD model, whereas the Jachimowski model gives a stable high frequency oscillation at 425-430 kHz. In contrast to the Mach 4.18 case, the Jachimowski model gives a better agreement with the experimental frequency at Mach 4.48.

Table 5. Comparison of the oscillation frequency

Frequency (kHz)	Ma = 4.18	Ma = 4.48
Experiment [3]	148	425
Jachimowski AUSM	160	425
Jachimowski Roe/HLL	165	430
UCSD-2016 AUSM	145	395
UCSD-2016 Roe/HLL	155	395

The test cases have shown that the mapped mesh solver developed in this work can predict the

oscillation of unsteady subdetonative shock-induced combustion. The numerical results are in good agreement with the experiments when a suitable reaction model is used.

In addition, a superdetonative case is simulated at Mach 5.04 using the Roe/HLL method and the Jachimowski mechanism. Several features are observed in this case compared with the previous subdetonative cases. As displayed in Figure 21, both the bow shock wave and reaction front are located away from the blunt body. The flame is closer to the bow shock, namely the induction length is shorter. The frequency of oscillation is much higher than that in the subdetonative case. The calculated frequency is 1155 kHz, which is slightly higher than the experimental value 1040 kHz.

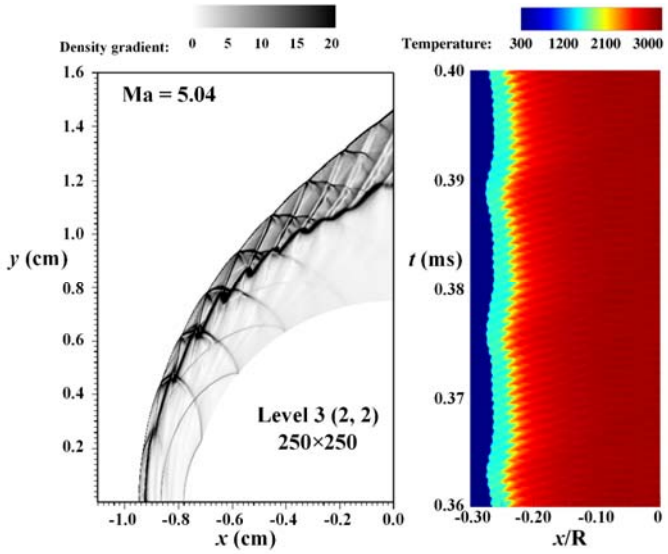

Figure 21. The density gradients distribution (left) and enlarged x-t diagram of temperature from 0.36 ms to 0.4 ms (right)

The present simulation of a superdetonative case is based on a similar mesh resolution as the previous subdetonative cases. Generally, a finer mesh is required to resolve the shorter induction region. However, the simulation is unstable when increasing the mesh resolution for the Mach 5.04 case. The reaction front is coupled with the bow shock wave, where a detonation is triggered. It has been reported that the inviscid solver cannot reproduce the results correctly at an extremely high resolution due to the loss of physical viscosities [19]. The error from the interactions of detailed chemical reactions is another possible reason for the unstable combustion [9].

As described, the chemical mechanism plays a vital role in predicting the correct oscillation. The physical viscosities are also important when the numerical mesh is refined to micrometer scale. The

effects of these factors on the unsteady shock-induced combustion process will be studied in the next development stage.

5. Conclusion

In this study, the Cartesian AMR framework AMROC-Clawpack was extended to enable AMR computations on a mapped, structured mesh. The main modifications include the coordinate transformation, the grid-aligned flux scheme, the MUSCL-Hancock method in physical space and restriction and prolongation operators for the adaptively refined mapped mesh. The mapped solver was tested using benchmark solutions for the multi-component compressible Euler equations. The numerical errors have been analysed with the method of manufactured solutions, which confirmed that the present solver can achieve second order on a mapped mesh. The mapped AMR solver was compared with the Cartesian AMR solver for shock tube, shock box and detonation problems. The solutions obtained by the present solver are in good agreement with published numerical results.

To validate the mapped solver, the unsteady shock-induced combustion problems were investigated using detailed chemistry mechanisms of hydrogen and air. The results show that the numerical pressure oscillation frequencies, the stand-off distance of the bow shock wave and the reaction front are in good agreement with results in the experiments and some previous numerical work. The developed solver provides a new approach to simulate the multi-species reactive problem on a non-Cartesian geometry in the AMROC-Clawpack framework. In the future, the viscosities for multi-species thermally perfect gases will be taken into account and the two-dimensional solver will be extended to three space dimensions for multi-species reactive problems.

Acknowledgments

The first author gratefully acknowledges financial support from China Scholarship Council (CSC). The authors also acknowledge the use of the IRIDIS High Performance Computing Facility, and associated support services at the University of Southampton, in the completion of this work.

Appendix. Analytical manufactured solution

The functions and parameters chosen for the manufactured solutions of Euler equations are given in Table A.

Table A. Constants for 2D Euler supersonic manufactured solution

ϕ	ϕ_0	ϕ_x	$f_{s,x}$	a_{ϕ_x}	ϕ_y	$f_{s,y}$	a_{ϕ_y}
ρY-O_2 (kg/m^3)	0.75	0.1	sin	1.0	0.2	cos	0.75
ρY-N_2 (kg/m^3)	1.0	-0.15	cos	0.5	0.1	cos	1.0
u (m/s)	800	60	sin	1.5	30	sin	0.75
v (m/s)	850	40	cos	1.0	50	sin	1.25
T (K)	1000	100	cos	1.0	75	cos	0.5

Reference

[1] Rubins, P. M., & Bauer, R. C. (1994). Review of shock-induced supersonic combustion research and hypersonic applications. Journal of Propulsion and Power, 10(5), 593-601.

[2] Choi, J. Y., Jeung, I. S., & Yoon, Y. (2000). Computational fluid dynamics algorithms for unsteady shock-induced combustion, part 1: validation. AIAA journal, 38(7), 1179-1187.

[3] Lehr, H. F. (1972). Experiments on shock-induced combustion. Astronautica Acta, 17, 589-597.

[4] McVey, J. B., & Toong, T. Y. (1971). Mechanism of instabilities of exothermic hypersonic blunt-body flows. Combustion Science and Technology, 3(2), 63-76.

[5] Matsuo, A., & Fujiwara, T. (1993). Numerical investigation of oscillatory instability in shock-induced combustion around a blunt body. AIAA journal, 31(10), 1835-1841.

[6] Wilson, G. J., & Sussman, M. A. (1993). Computation of unsteady shock-induced combustion using logarithmic species conservation equations. AIAA journal, 31(2), 294-301.

[7] Matsuo, A., Fujii, K., & Fujiwara, T. (1995). Flow features of shock-induced combustion around projectile traveling at hypervelocities. AIAA journal, 33(6), 1056-1063.

[8] Yungster, S., Eberhardt, S., & Bruckner, A. P. (1991). Numerical simulation of hypervelocity projectiles in detonable gases. AIAA journal, 29(2), 187-199.

[9] Yuan, L., & Tang, T. (2007). Resolving the shock-induced combustion by an adaptive mesh redistribution method. Journal of Computational Physics, 224(2), 587-600.

[10] Deiterding, R. (2009). A parallel adaptive method for simulating shock-induced combustion with detailed chemical kinetics in complex domains. Computers & Structures, 87(11-12), 769-783.

[11] Li, B., & Yuan, L. (2013). Convergence issues in using high‐resolution schemes and lower–upper symmetric Gauss–Seidel method for steady shock‐induced combustion problems. International Journal for Numerical Methods in Fluids, 71(11), 1422-1437.

[12] Dong, H., Zhang, F., Xu, C., & Liu, J. (2018). An improved uncoupled finite volume solver for simulating unsteady shock-induced combustion. Computers & Fluids, 167, 146-157.

[13] Kim, S. L., Choi, J. Y., Jeung, I. S., & Park, Y. H. (2001). Application of approximate chemical Jacobians for constant volume reaction and shock-induced combustion. Applied numerical mathematics, 39(1), 87-104.

[14] Kumar, P. P., Kim, K. S., Oh, S., & Choi, J. Y. (2015). Numerical comparison of hydrogen-air reaction mechanisms for unsteady shock-induced combustion applications. Journal of Mechanical Science and Technology, 29(3), 893-898.

[15] Pavalavanni, P. K., Sohn, C. H., Lee, B. J., & Choi, J. Y. (2019). Revisiting unsteady shock-induced combustion with modern analysis techniques. Proceedings of the Combustion Institute, 37(3), 3637-3644.

[16] Berger, M. J., & Oliger, J. (1984). Adaptive mesh refinement for hyperbolic partial differential equations. Journal of computational Physics, 53(3), 484-512.

[17] Berger, M. J., & Colella, P. (1989). Local adaptive mesh refinement for shock hydrodynamics. Journal of computational Physics, 82(1), 64-84.

[18] Deiterding, R., (2003). Parallel adaptive simulation of multi-dimensional detonation structures. PhD thesis, Brandenburg University of Technology Cottbus–Senftenberg, Cottbus

[19] Ziegler, J. L., Deiterding, R., Shepherd, J. E., & Pullin, D. I. (2011). An adaptive high-order hybrid scheme for compressive, viscous flows with detailed chemistry. Journal of Computational Physics, 230(20), 7598-7630.

[20] Peng, H., Huang, Y., Deiterding, R., Luan, Z., Xing, F., & You, Y. (2018). Effects of jet in crossflow on flame acceleration and deflagration to detonation transition in methane–oxygen mixture. Combustion and Flame, 198, 69-80.

[21] Wei, H., Zhang, X., Zeng, H., Deiterding, R., Pan, J., & Zhou, L. (2019). Mechanism of end-gas autoignition induced by flame-pressure interactions in confined space. Physics of Fluids, 31(7), 076106.

[22] Cai, X., Deiterding, R., Liang, J., Sun, M., & Mahmoudi, Y. (2018). Diffusion and mixing

effects in hot jet initiation and propagation of hydrogen detonations. Journal of Fluid Mechanics, 836, 324-351.

[23] Wang, Y., Han, W., Deiterding, R., & Chen, Z. (2018). Effects of disturbance on detonation initiation in H 2/O 2/N 2 mixture. Physical Review Fluids, 3(12), 123201.

[24] Barraza, J. A. R., & Deiterding, R. (2020). Towards a generalised lattice Boltzmann method for aerodynamic simulations. Journal of Computational Science, 45, 101182.

[25] Atkins, C., & Deiterding, R. (2020). Towards a Strand-Cartesian Solver for Modelling Hypersonic Flows in Thermochemical Non-Equilibrium. In 23rd AIAA International Space Planes and Hypersonic Systems and Technologies Conference.

[26] Yu, S. T. (1993). Convenient method to convert two-dimensional CFD codes into axisymmetric ones. Journal of Propulsion and Power, 9(3), 493-495.

[27] Kee, R. J., Rupley, F. M., & Miller, J. A. (1989). Chemkin-II: A Fortran chemical kinetics package for the analysis of gas-phase chemical kinetics (No. SAND-89-8009). Sandia National Lab. (SNL-CA), Livermore, CA (United States).

[28] LeVeque, R. J. (2002). Finite volume methods for hyperbolic problems (Vol. 31). Cambridge university press.

[29] Liou, M. S., & Steffen Jr, C. J. (1993). A new flux splitting scheme. Journal of Computational physics, 107(1), 23-39.

[30] Toro, E. F. (2013). Riemann solvers and numerical methods for fluid dynamics: a practical introduction. Springer Science & Business Media.

[31] Deiterding, R. (2011, December). Block-structured adaptive mesh refinement-theory, implementation and application. In Esaim: Proceedings (Vol. 34, pp. 97-150). EDP Sciences.

[32] Berger, M. J., & LeVeque, R. J. (1998). Adaptive mesh refinement using wave-propagation algorithms for hyperbolic systems. SIAM Journal on Numerical Analysis, 35(6), 2298-2316.

[33] Calhoun, D., & LeVeque, R. J. (2005). An accuracy study of mesh refinement on mapped grids. In Adaptive Mesh Refinement-Theory and Applications (pp. 91-101). Springer, Berlin, Heidelberg.

[34] Press, W.H., William, H., Teukolsky, S.A., Vetterling, W.T., Saul, A. and Flannery, B.P., (2007). Numerical recipes 3rd edition: The art of scientific computing. Cambridge university press, Cambridge.

[35] Hoffmann, K. A., & Chiang, S. T. (2000). Computational fluid dynamics volume I. Engineering Education System.

[36] Persson, P. O., Bonet, J., & Peraire, J. (2009). Discontinuous Galerkin solution of the Navier–Stokes equations on deformable domains. Computer Methods in Applied Mechanics and Engineering, 198(17-20), 1585-1595.

[37] Salari, K., & Knupp, P. (2000). Code verification by the method of manufactured solutions (No. SAND2000-1444). Sandia National Labs., Albuquerque, NM (US); Sandia National Labs., Livermore, CA (US).

[38] Roy, C. J., Nelson, C. C., Smith, T. M., & Ober, C. C. (2004). Verification of Euler/Navier–Stokes codes using the method of manufactured solutions. International Journal for Numerical Methods in Fluids, 44(6), 599-620.

[39] Fedkiw, R. P. (1997). A survey of chemically reacting, compressible flows. PhD thesis, University of California, Los Angeles.

[40] Ferrer, P. J. M., Buttay, R., Lehnasch, G., & Mura, A. (2014). A detailed verification procedure for compressible reactive multicomponent Navier–Stokes solvers. Computers & Fluids, 89, 88-110.

[41] Owen, L. D., Guzik, S. M., & Gao, X. (2018). A high-order adaptive algorithm for multispecies gaseous flows on mapped domains. Computers & Fluids, 170, 249-260.

[42] Westbrook, C. K. (1982). Chemical kinetics of hydrocarbon oxidation in gaseous detonations. Combustion and Flame, 46, 191-210.

[43] Goodwin, D. G., Speth, R. L., Moffat, H. K., & Weber, B. W. (2018) Cantera: An object-oriented software toolkit for chemical kinetics, thermodynamics, and transport processes.

[44] Browne, S., Ziegler, J., & Shepherd, J. E. (2008). Numerical solution methods for shock and detonation jump conditions. GALCIT report FM2006, 6, 90.

[45] Gavrikov, A. I., Efimenko, A. A., & Dorofeev, S. B. (2000). A model for detonation cell size prediction from chemical kinetics. Combustion and flame, 120(1-2), 19-33.

[46] Kaneshige, M., & Shepherd, J. E. (1997). Detonation database.

[47] Oran, E. S., Weber Jr, J. W., Stefaniw, E. I., Lefebvre, M. H., & Anderson Jr, J. D. (1998). A numerical study of a two-dimensional H2-O2-Ar detonation using a detailed chemical reaction model. Combustion and Flame, 113(1-2), 147-163.

[48] Hu, X. Y., Zhang, D. L., Khoo, B. C., & Jiang, Z. L. (2005). The structure and evolution of a two-dimensional H2/O2/Ar cellular detonation. Shock Waves, 14(1-2), 37-44.

[49] Fickett, W., & Davis, W. C. (2000). Detonation: theory and experiment. Courier Corporation.

[50] Jachimowski, C. J. (1988). An analytical study of the hydrogen-air reaction mechanism with application to scramjet combustion. Technical Report No. NASA TP-2791.

[51] Yungster, S., & Radhakrishnan, K. (1996). A fully implicit time accurate method for hypersonic combustion: application to shock-induced combustion instability. Shock Waves, 5(5), 293-303.

[52] Teng, H., Liu, S., & Zhang, Z. (2020). Unsteady combustion mode with a super-high frequency induced by a curved shock. Physics of Fluids, 32(11), 116101.

[53] Chemical-kinetic mechanisms for combustion applications. (2016). San Diego Mechanism web page, Mechanical and Aerospace Engineering (Combustion Research), University of California at San Diego (http://combustion.ucsd.edu).